

# Interfacial Anion-Induced Dispersion of Active Species for Efficient Electrochemical Baeyer–Villiger Oxidation

Shuangshuang Cha,<sup>†</sup> Yuxin Chen,<sup>†</sup> Wei Du, Jianxiang Wu, Ran Wang, Tao Jiang, Xuejing Yang, Cheng Lian,<sup>\*</sup> Honglai Liu, and Ming Gong<sup>\*</sup>



Cite This: *JACS Au* 2024, 4, 3629–3640



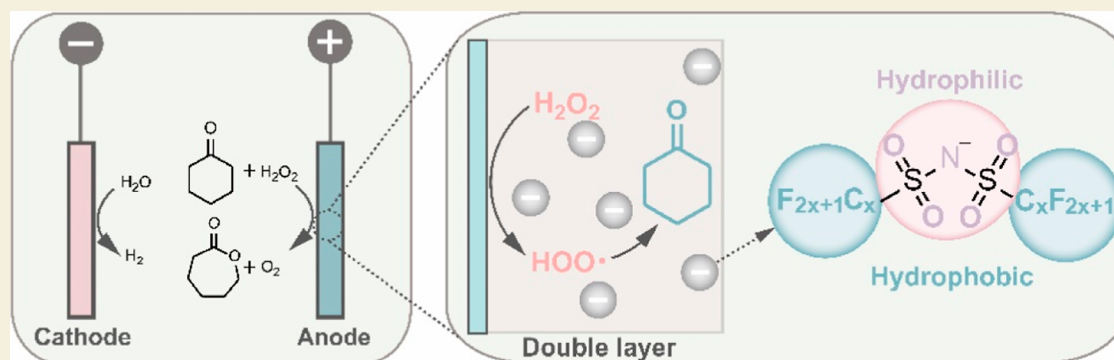
Read Online

ACCESS |

Metrics & More

Article Recommendations

Supporting Information



**ABSTRACT:** Degradable polymers are an effective solution for white plastic pollution. Polycaprolactone is a type of degradable plastic with desirable mechanical and biocompatible properties, and its monomer,  $\epsilon$ -caprolactone ( $\epsilon$ -CL), is often synthesized by Baeyer–Villiger (B–V) oxidation that demands peroxyacids with low safety and low atom-efficiency. Herein, we devised an electrochemical B–V oxidation system simply driven by  $\text{H}_2\text{O}_2$  for the efficient production of  $\epsilon$ -CL. This system involves two steps with the direct oxidation of  $\text{H}_2\text{O}_2$  into  $\bullet\text{OOH}$  radicals at the electrode surface and the indirect oxidation of cyclohexanone by the generated reactive oxygen species. The modulation of the interfacial ionic environment by amphiphilic sulfonimide anions [e.g., bis(trifluoromethane)sulfonimide ( $\text{TFSI}^-$ )] is highly critical. It enables the efficient B–V oxidation into  $\epsilon$ -caprolactone with  $\sim 100\%$  selectivity and 68.4% yield at a potential of 1.28 V vs RHE, much lower than the potentials applied for electrochemical B–V oxidation systems using water as the O sources. On hydrophilic electrodes with the action of sulfonimide anions, hydrophilic  $\text{H}_2\text{O}_2$  can be enriched within the double layer for direct oxidation while hydrophobic cyclohexanone can be simultaneously accumulated for rapidly reacting with the reactive oxygen species. This work not only enriches the electrified method of the ancient B–V oxidation by using only  $\text{H}_2\text{O}_2$  toward monomer production of biodegradable plastics but also emphasizes the critical role of the interfacial ionic environment for electrosynthesis systems that may extend the scope of activity optimization.

**KEYWORDS:** Baeyer–Villiger oxidation, ionic environment, electrochemical oxidation, amphiphilic anion, caprolactone

## INTRODUCTION

As one of the most important end products in the petrochemical industry, plastics have been used extensively in daily lives due to their remarkable durability, lightness, stability, and low cost.<sup>1</sup> The global annual consumption of plastics reaches 300 million tons, of which nondegradable plastics account for  $>99\%$  that raises significant environmental and sustainability problems.<sup>2–5</sup> To sustain our lives on polymers, the development of recyclable or degradable polymers has been a central focus of research in recent years.<sup>6,7</sup> Polyester is a class of degradable plastics that has received widespread attention owing to the low melting point, good thermal processability, and low viscosity. Among all polyesters, polycaprolactone, typically polymerized from  $\epsilon$ -caprolactone, possesses excellent rheological and viscoelastic

properties.<sup>8</sup> Its high biocompatibility, biodegradability, and nontoxicity also grant its vast biomedical applications in drug delivery, implants, tissue engineering, adhesives, etc.<sup>9,10</sup>

$\epsilon$ -Caprolactone ( $\epsilon$ -CL), the monomer of polycaprolactone, can be synthesized via various routes, including 1,6-hexanediol dehydrogenation, 6-hydroxycaproic acid intramolecular condensation, and oxidation of cyclohexanone.<sup>2,11</sup> Among them, Baeyer–Villiger (B–V) oxidation via directly inserting one

Received: July 2, 2024

Revised: July 27, 2024

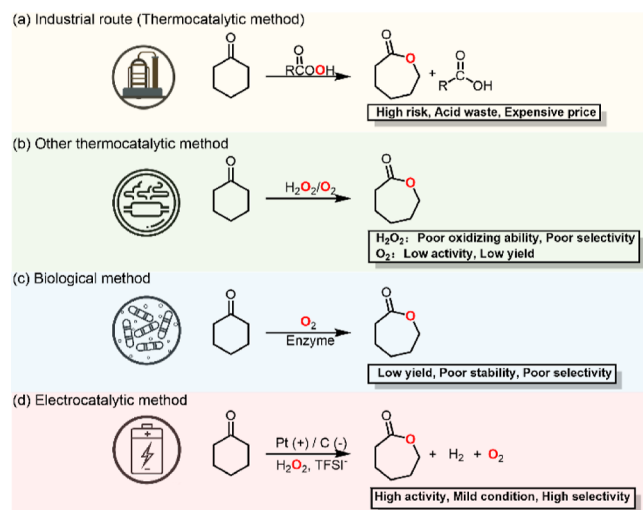
Accepted: August 2, 2024

Published: September 5, 2024



oxygen atom into ketone using peroxyacids is the most commonly used method.<sup>12</sup> On an industrial scale,  $\epsilon$ -caprolactone is produced by mixing cyclohexanone with peracetic acid (Scheme 1a). Despite the high reaction

### Scheme 1. Scheme of the Different Routes of $\epsilon$ -Caprolactone Production and Their Advantages/Disadvantages



efficiency, peracetic acid is generally a mixture of acetic acid, hydrogen peroxide ( $\text{H}_2\text{O}_2$ ), and water, with low content of active materials and high explosiveness that often needs a stabilizing agent for storage.<sup>13</sup> Furthermore, the stoichiometric byproducts of peroxyacids are low-value chemicals requiring additional downstream separation processes.<sup>14–16</sup> These issues not only result in extremely high production costs of  $\epsilon$ -CL but also cause environmental and safety concerns that limit the scale of industrial applications.

In contrast to the peroxyacid route,  $\text{H}_2\text{O}_2$  is a more benign oxidant with water as the only byproduct (Scheme 1b).<sup>17</sup>  $\text{H}_2\text{O}_2$  also contains a higher concentration of reactive oxygen species (47 wt %) with high atom utilization efficiency. These advantages not only improve the economic benefits but also reduce wastewater production and separation cost.<sup>18,19</sup> However, activating  $\text{H}_2\text{O}_2$  to achieve a high oxidizing capability with high selectivity toward B–V oxidation is a grand challenge. Typically, a solid catalyst is required to activate the nucleophilic properties of  $\text{H}_2\text{O}_2$ .<sup>20,21</sup> For instance, tin-based catalysts are often used to activate  $\text{H}_2\text{O}_2$  to efficiently catalyze the B–V oxidation of ketones, but this catalyst often has problems such as easy deactivation of active sites and high temperatures required for the reaction.<sup>21</sup> Another strategy is to use molecular oxygen as an oxidant, which could achieve higher safety and lower costs (Scheme 1b). Nevertheless, activating the O–O bond in molecular oxygen is a crucible. Currently, co-oxidants and stoichiometric aldehydes are demanded to achieve  $\text{O}_2$ -driven B–V oxidation with high selectivity. These coadditives effectively generate peroxyacids in situ for realizing B–V reactivity, but the excessive side products and co-oxidants require high separation cost, or they would affect the texture properties of plastic products. Biocatalysis is another route of achieving  $\text{O}_2$ -driven B–V oxidation (Scheme 1c).<sup>22</sup> Baeyer–Villiger monoxygenases are a newly developed class of biocatalysts that can selectively oxidize ketones using oxygen under mild conditions.<sup>23–25</sup>

Although many Baeyer–Villiger monoxygenases have been reported, it is still very difficult to massively use in industry, mainly due to their poor thermal and chemical stability under industrial conditions.<sup>23,26</sup>

To date,  $\text{H}_2\text{O}_2$  is still the most viable oxidant to address the problem of the peroxyacid pathway in industry. Electrosynthesis is an emerging technology that enables the in situ generation of active species for selective synthetic processes.  $\text{H}_2\text{O}_2$  can be anodized into various reactive oxygen species via electron transfers or proton-coupled electron transfers for targeted oxidation reactions. Meanwhile, it can be paired with the cathodic production of hydrogen, which is a high-value energy carrier in the context of hydrogen economy.<sup>27</sup> Compared to the recent studies on using water as the O sources for electrochemical B–V oxidation,<sup>28,29</sup>  $\text{H}_2\text{O}_2$  can be activated at much lower overpotentials into the desired reactive oxygen species, offering more efficient electrosynthesis systems. Currently, the strategies of improving the effectiveness toward electrochemical  $\text{H}_2\text{O}_2$  activation is based on advanced catalyst structures, which can be applied to various oxidation reactions including organic oxidation and pollutant removal.<sup>30–35</sup> However, the composition of the electrode/electrolyte interface where  $\text{H}_2\text{O}_2$  activation and B–V oxidation occur is also a key factor affecting the reactivity.<sup>36,37</sup> Various reactants, ions, solvents, and additives can coexist near the electrode/electrolyte interface and significantly influence the detailed reaction pathway, for instance, the identity of  $\text{H}_2\text{O}_2$  oxidation intermediate and its subsequent reaction with cyclohexanone. Designing the electrode/electrolyte compositions and unveiling the microscopic picture of the electrode/electrolyte interface, especially for electrosynthesis, not only enables the mechanistic understanding of the reaction pathway but also expedites the rational optimization of electrosynthetic conditions toward more efficient electrochemical processes and is thus highly desired.

In this work, we realize the  $\text{H}_2\text{O}_2$ -driven electrochemical conversion of cyclohexanone into  $\epsilon$ -CL using a Pt anode in an acetonitrile/water mixed electrolyte, accompanied by the coproduction of high-purity hydrogen on the cathode (Scheme 1d). This reaction path involves the direct oxidation of  $\text{H}_2\text{O}_2$ , a hydrophilic pathway, and the indirect oxidation of cyclohexanone, a hydrophobic pathway. Constructing the hydrophilic/hydrophobic coexistent interface is a key to realize this path, and to this end, we utilize the bis(trifluoromethane)sulfonimide (TFSI<sup>−</sup>) anion with both hydrophilic and hydrophobic domains to tune the interfacial structure. The hydrophilic part can attract  $\text{H}_2\text{O}_2$  to the electrode surface for oxidation into reactive oxygen species while the hydrophobic part can encourage the accumulation of cyclohexanone near the interface for reacting with reactive oxygen species in time to generate  $\epsilon$ -CL. A high  $\epsilon$ -CL yield (~68%) and a high selectivity (~100%) can be achieved via this electrochemical process with 0.1 M TFSI<sup>−</sup> in the acetonitrile/water = 1:1 electrolyte under low overpotentials. The effects of the acetonitrile to water ratio, ion hydrophilicity (or hydrophobicity), electrode hydrophilicity (or hydrophobicity), and ion concentration were systematically studied using electrochemical kinetics, in situ spectroscopy, and molecular dynamics (MD). The coexistent hydrophilicity and hydrophobicity of TFSI<sup>−</sup> is demonstrated to be essential for breaking the solvent-rich domains, allowing the access of both  $\text{H}_2\text{O}_2$  and cyclohexanone to the electrode interface for B–V oxidation. The microscopic picture of reactant and ion distribution near

the interface is depicted in detail, offering new insights about the species homogeneity at the electrode/electrolyte interface.

## RESULTS AND DISCUSSION

### Reaction Pathway of the H<sub>2</sub>O<sub>2</sub>-Driven Electrochemical B–V Oxidation

We first studied the reaction mechanism of the electrochemical B–V oxidation in a molecular aspect, and such an understanding can offer valuable insights into the optimization and analysis of interfacial structures on this process. Before the detailed mechanistic study, we briefly screened the electrode materials and reaction conditions that can be sustained under mixed organic/aqueous solvents and neutral conditions. Platinum (Pt) and carbon-fiber paper (CP) electrode outperformed other electrodes, in terms of  $\epsilon$ -CL yield (Figure S1). Although Pt is much more expensive, it can oxidize H<sub>2</sub>O<sub>2</sub> at a much lower overpotential (Figure S2), which is much lower than the potential required for water oxidation into reactive oxygen species, and therefore, Pt is utilized for the mechanistic study. A constant current electrolysis at 10 mA/cm<sup>2</sup> was also utilized as the standard condition (Figure S3).

In thermocatalysis, Sn-based catalysts are often used to activate H<sub>2</sub>O<sub>2</sub>. Specifically, H<sub>2</sub>O<sub>2</sub> first attacks the Brønsted base sites to form Sn hydroperoxide (SnOOH) as the active species.<sup>38</sup> Meanwhile, the Sn-based catalyst can activate the carbonyl group of the ketone, thereby enhancing the electrophilicity of the ketone.<sup>39</sup> However, in our electrocatalytic system, there are no Brønsted base sites in either Pt or CP electrodes; therefore, we speculate that the mechanism might be different in electrocatalysis from thermocatalysis.

We first carried out a systematic study of different control groups to glean the active species during the electrochemical B–V oxidation (Figure 1a). Under the standard conditions, a single product of  $\epsilon$ -CL (52.1%) with an extremely high selectivity (~100%) could be obtained by activating H<sub>2</sub>O<sub>2</sub> with an electric potential for 3 h. Prolonging the electrolysis could generate a maximal yield of 68.4%, and an isolated yield of 54.4% with 372.5 mg of  $\epsilon$ -CL product could be obtained. Similar yields could be obtained by electrolysis at 1.55 V vs RHE and a volcanic dependence of yields on potentials was observed, likely due to the presence of side reactions at higher potentials (Figure S4). Without applying the potential, we could not detect any product, which implies that the oxidation activity of H<sub>2</sub>O<sub>2</sub> itself is not sufficient to achieve B–V oxidation without any electric drive. The same result was obtained in the absence of H<sub>2</sub>O<sub>2</sub>, demonstrating the inability of water oxidation as the oxygen source. In thermocatalysis, there are mainly three ways of activating H<sub>2</sub>O<sub>2</sub>: (1) dissociative ionization into H<sup>+</sup> and OOH<sup>-</sup>, (2) heterocleavage of H<sub>2</sub>O<sub>2</sub> to form  $\bullet$ H and  $\bullet$ OOH radicals, and (3) homocleavage of the O–O bond to form two  $\bullet$ OH radicals. To verify the active oxygen species, we carried out control experiments to compare. First, we added 0.01 M potassium hydroxide (KOH) to expedite the ionization of H<sub>2</sub>O<sub>2</sub> into OOH<sup>-</sup>. Without any applied potential, we could not detect any  $\epsilon$ -CL. Even under the identical potential applied, we observed a significantly decreased  $\epsilon$ -CL yield of only 23.1%, compared to 52.1%, excluding the significant contribution of facilitated OOH<sup>-</sup> generation in electrochemical systems. Additionally, under more alkaline conditions,  $\epsilon$ -CL can be easily hydrolyzed into 6-hydroxycaproic acid or 6-hydroxycaproic acid salt (with a yield of 19.13%), resulting in a declined selectivity. As a

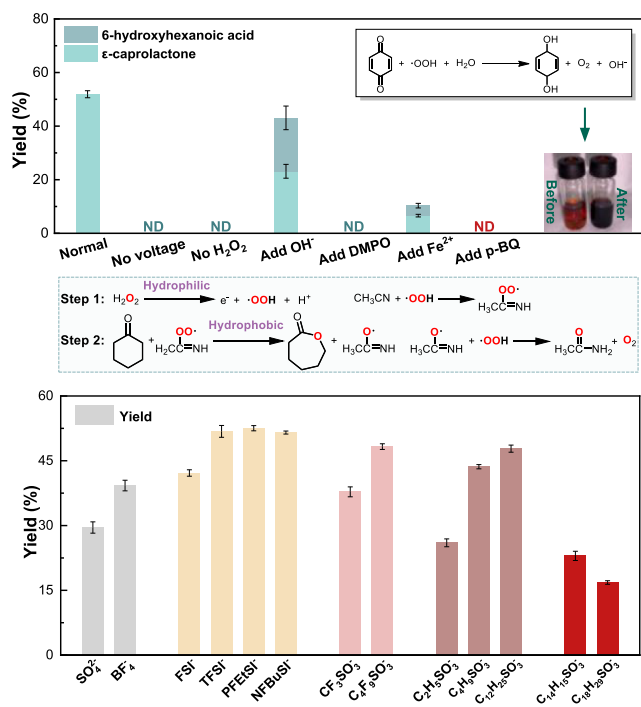


**Figure 1.** (a) Yield of  $\epsilon$ -caprolactone or 6-hydroxyhexanoic acid during electrochemical B–V oxidation under different control groups. (b) Proposed mechanism of electrochemical B–V oxidation of cyclohexanone. (c) Yield of  $\epsilon$ -caprolactone under the electrolytes with different anions. Standard conditions: Pt electrode, 10 mA/cm<sup>2</sup>, 3 h, and anodic polarization.

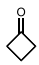
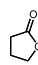
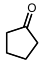
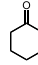
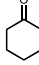
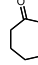
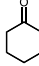
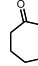
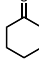
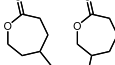
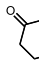
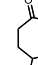
consequence, H<sub>2</sub>O<sub>2</sub> activation likely undergoes a radical pathway.

To confirm the radical formation, we first added DMPO to capture the free radicals generated during the electrolysis. With the addition of DMPO, no  $\epsilon$ -CL product was detected. To determine the identity of free radicals, we further added ferrous ions (Fe<sup>2+</sup>) and 1,4-benzoquinone (p-BQ) to the system. Fe<sup>2+</sup> can expedite the Fenton reaction to generate  $\bullet$ OH radicals,<sup>40</sup> and if the  $\bullet$ OH radical is the key to B–V oxidation, then the yield might be improved. In fact, upon Fe<sup>2+</sup> addition, the  $\epsilon$ -CL yield drastically decreased to ~6.6%, accompanied by ~3.7% yield of 6-hydroxycaproic acid or its salt, which suggests that  $\bullet$ OH is not a significant contributor in the pathway. Additionally, p-BQ is a selective quencher of  $\bullet$ OOH radicals.<sup>41</sup> Upon p-BQ addition, we again detected no  $\epsilon$ -CL product, which demonstrated that the active oxygen species might be  $\bullet$ OOH. In electrochemical systems, the generation of  $\bullet$ OOH radicals is not likely through heterocleavage with coproduced  $\bullet$ H but instead through the electrochemical oxidation of H<sub>2</sub>O<sub>2</sub> via proton-coupled electron transfer or first deprotonation of H<sub>2</sub>O<sub>2</sub> and then single-electron oxidation. Moreover, the acetonitrile is another essential component for the electrochemical B–V oxidation. When the reaction was carried out in a 1,4-dioxane/water mixed solvent, no  $\epsilon$ -CL product was detected (Figure S5). The use of acetonitrile in thermocatalytic B–V oxidation or epoxidation has been extensively discussed in the literature, and its role in the electrochemical system is very similar. The detection of acetamide byproduct in GC–MS further confirmed the utility of acetonitrile (Figure S6), and almost one equivalent of acetamide could be detected by HPLC (Figure S7).

Overall, the proposed mechanism in our electrochemical B–V oxidation undergoes two major steps (Figure 1b).  $\text{H}_2\text{O}_2$  is first oxidized into  $\bullet\text{OOH}$  via loss of protons and electrons on the electrode, and this  $\bullet\text{OOH}$  radical is efficiently trapped by acetonitrile to form peroxyacetonitrile free radicals. This peroxyacetonitrile free radical is the active species that can further attack cyclohexanone and rearrange to form  $\epsilon$ -CL in a B–V oxidation manner, and during this process, the leaving group further reacts with the  $\bullet\text{OOH}$  radical or peroxyacetonitrile to form the acetamide and  $\text{O}_2$  to complete the cycle. Interestingly, from the aspect of the interface, the two steps involved here can be categorized into the hydrophilic process of direct  $\text{H}_2\text{O}_2$  oxidation and the hydrophobic process of indirect oxidation of cyclohexanone via peroxyacetonitrile. Therefore, we speculate that regulating the hydrophilicity and hydrophobicity of the interface may have a significant impact on the activity, thereby maximizing the yield of  $\epsilon$ -CL.

A major component of the electrode–electrolyte interface is the ions. Since the reaction is carried out under anodic potentials and anions are accumulated near the interface, we first examined the effect of the anion hydrophilicity and hydrophobicity on the  $\epsilon$ -CL yield (Figure 1c). The hydrophilicity and hydrophobicity were first qualitatively governed by the anion structures, in which the longer C–H or C–F tails indicate stronger hydrophobicity (Figure S8). Generally, as the hydrophobicity of the anion increases, the  $\epsilon$ -CL yield increases, but further increasing the length of hydrophobic tails only cast negative effects on the yield. Compared with simple hydrophilic anions ( $\text{SO}_4^{2-}$ ), fluorine-containing anions ( $\text{BF}_4^-$ ) can possess higher hydrophobicity that may accelerate the second step of B–V oxidation on cyclohexanone, such that the active species is consumed in a timely manner without degrading into oxygen. As a consequence, the  $\epsilon$ -CL yield increased from 29.54% of  $\text{SO}_4^{2-}$  to 39.26% of  $\text{BF}_4^-$ . The more fluorine atoms, the more hydrophobic the anions, and the more obvious increase in the  $\epsilon$ -CL yield ( $\text{FSI}^- < \text{TFSI}^- < \text{NFBuSI}^-$ ) ( $\text{CF}_3\text{SO}_3^- < \text{C}_4\text{F}_9\text{SO}_3^-$ ). The same trend can be applied to pure alkyl chains. However, when the anion bears a benzene ring group or is too hydrophobic that may form micelles, it led to a decrease in  $\epsilon$ -CL yield that may affect the first step of  $\text{H}_2\text{O}_2$  oxidation ( $\text{C}_{14}\text{H}_{15}\text{SO}_3^- > \text{C}_{18}\text{H}_{29}\text{SO}_3^-$ ). Among these anions, the sulfonimide anions exhibited the best performances. According to their structures, these ions include both hydrophilic and hydrophobic domains (Figure S9), in which the hydrophilic domain is conducive to the direct  $\text{H}_2\text{O}_2$  oxidation on the electrode surface, and its hydrophobic domain is conducive to the accumulation of cyclohexanone near the interface for B–V oxidation. Comparatively, the cations negligibly influence the B–V oxidation performance (Figure S10). This interfacial hydrophobic effect can also be further expanded to other cyclic ketone systems (Table 1 and Figure S11) but extending to other linear ketones still remains a great challenge. Unfortunately, due to the presence of  $\text{H}_2\text{O}_2$  degradation and oxidation by-pathway to  $\text{O}_2$ , excessive reaction time and overdosage of  $\text{H}_2\text{O}_2$  were demanded to achieve the high yields, which led to the limitation in the unsatisfactory Faradaic efficiency and oxygen atom-efficiency (Table S1) that needs further optimization to realize highly efficient synthetic systems. This strategy may also provide a reference for other systems with both hydrophilic and hydrophobic substrates. Since  $\text{TFSI}^-$  has one of the highest  $\epsilon$ -CL yields and further increasing the hydrophobic tails has no

**Table 1. Electrolytic Products and Corresponding Yields and Selectivity of Various Substrates<sup>a</sup>**

Entry	Substrate	Product	Yield (%)	Selectivity (%)
1			88.46	100
2			25.06	100
3			68.40	100
4			41.44	100
5			26.10/20.49	56.02/43.98
6			60.54	100

<sup>a</sup>Electrolytic conditions: 60 mM substrate + 720 mM  $\text{H}_2\text{O}_2$  + 0.1 M LiTFSI, acetonitrile/water = 1:1, Pt as the catalyst, and a constant current of 10 mA for 6 h.

significant increase in yield, we mostly use  $\text{TFSI}^-$  as a standard ion in the following study.

#### Co-effect of Anion and Electrode Hydrophilicity and Hydrophobicity

In addition to the anions, the hydrophilicity and hydrophobicity of the electrode are other important components that govern the property of the interface. Accordingly, we examined the effect of different anode materials under different salts to glean the hydrophilicity and hydrophobicity effect (Figure 2a). Both hydrophilic metal electrodes [Pt, titanium (Ti) mesh, and stainless steel (SS)] and hydrophobic carbon electrodes [CP and graphite plate (GP)] were utilized. On all hydrophilic electrodes (Pt, Ti, and SS), the  $\epsilon$ -CL yields increase as the hydrophobicity of the anions increases (Figures 2b and S12). The general trend of  $\epsilon$ -CL follows Pt > Ti > SS. These hydrophilic interfaces usually have some hydroxyl groups that interact very weakly with cyclohexanone but very strongly with  $\text{H}_2\text{O}$ , so that the accumulation of the cyclohexanone near the interface is rather difficult. With the hydrophobic anions electrostatically accumulated near the interface, they may attract cyclohexanone via hydrophobic forces to the interface, thus promoting downstream B–V oxidation with the reactive oxygen species. On the contrary, the hydrophobic electrodes exhibited much smaller dependence on the hydrophobicity of the anions because the hydrophobicity of the electrode is sufficient to accumulate the cyclohexanone substrate without the need of assistance from the anions. In such scenarios, the first step of  $\text{H}_2\text{O}_2$  oxidation may determine the activity. A relatively more hydrophilic CP electrode with surface defects outperformed the purely hydrophobic GP electrode. Therefore, the hydrophilicity and hydrophobicity of the anions and electrode together govern the overall performance of the  $\text{H}_2\text{O}_2$ -driven electrochemical B–V oxidation.

To glean the co-effect of the electrode and anion, we measured the electrochemical kinetics on two representative

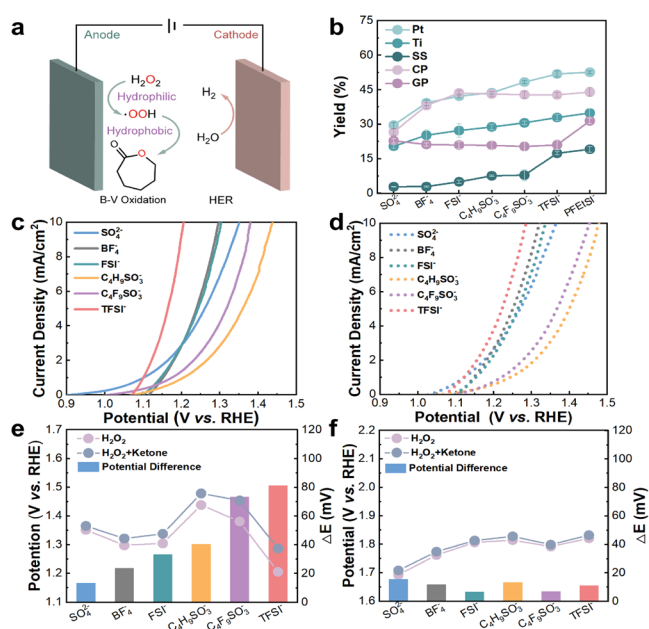


**Figure 2.** (a) Schematic diagram of electrochemical B–V oxidation of cyclohexanone. (b) Yield of  $\epsilon$ -caprolactone under the electrolytes with different anions on different electrodes. (c,d) Polarization curves of the Pt electrode under different anions (c) without and (d) with cyclohexanone. The scan rate is 10 mV/s. (e,f) Potentials and potential differences of H<sub>2</sub>O<sub>2</sub> oxidation at 10 mA/cm<sup>2</sup> with and without cyclohexanone on the (e) Pt electrode and (f) CP electrode.

electrodes of the hydrophilic Pt and hydrophobic CP. Specifically, the H<sub>2</sub>O<sub>2</sub> oxidation kinetics were compared with and without the addition of cyclohexanone (Figure 2c,d). For most anions, the polarization curves start off from 1.0 to 1.1 V vs RHE with increasing current at higher overpotentials, corresponding to the electro-oxidation of H<sub>2</sub>O<sub>2</sub>. These potentials were much more negative than the water oxidation potential, suggesting the much expedited kinetics of H<sub>2</sub>O<sub>2</sub> oxidation (Figure S13). In the cases with certain anions (e.g., BF<sub>4</sub><sup>-</sup>, FSI<sup>-</sup>, and TFSI<sup>-</sup>), the current was negative at more negative potentials, suggesting the presence of reduction current. This current was presumably due to the reduction of O<sub>2</sub> or other reactive oxygen species generated during the decomposition of H<sub>2</sub>O<sub>2</sub>. The presence of this reduction current could interfere with the analysis of onset potential but not with the following analysis on H<sub>2</sub>O<sub>2</sub> oxidation current. The major differences among different anions are the current growing speed (or Tafel slope) and the potential at a relatively high current density (e.g., 10 mA/cm<sup>2</sup>).

The TFSI<sup>-</sup> anion showed the largest current growth and the lowest overpotential at 10 mA/cm<sup>2</sup>. Since only H<sub>2</sub>O<sub>2</sub> is present and the identical Pt electrode was used in this experiment, the higher H<sub>2</sub>O<sub>2</sub> oxidation current suggests a higher affinity toward H<sub>2</sub>O<sub>2</sub> at the interface, which likely relates to the hydrophilic properties of the anions. Upon the addition of cyclohexanone, the H<sub>2</sub>O<sub>2</sub> oxidation current apparently decreased for all anions. Again, the potentials at relatively low current densities remained almost unchanged for different anions and with/without cyclohexanone, suggesting that the intrinsic kinetics is not much affected and is only correlated with the nature of the catalyst electrode and H<sub>2</sub>O<sub>2</sub>. Still, a current density of 10 mA/cm<sup>2</sup> can be achieved at a low potential of 1.28 vs RHE, demonstrating a high energy efficiency. The anions and cyclohexanone affected the amount of available H<sub>2</sub>O<sub>2</sub> at the

local interface. Thus, the addition of cyclohexanone decreased the current increase by occupying some of the spaces near the interface. The more hydrophobic anions, the more facile the accumulation of cyclohexanone at the interface, thereby decreasing the H<sub>2</sub>O<sub>2</sub> oxidation current by a larger extent. We analyzed the potentials required to reach 10 mA/cm<sup>2</sup> for different anions (Figure 2e), and we utilized the difference with and without cyclohexanone as a descriptor of the local hydrophobicity. In spite of the varying trend of the H<sub>2</sub>O<sub>2</sub> oxidation current itself, this potential difference scales well with the anion hydrophobicity, as well as the  $\epsilon$ -CL yield. It suggests that the local accumulation of cyclohexanone at the interface could be the key to the  $\epsilon$ -CL yield via electrochemical B–V oxidation. It is also worthwhile to note that although the TFSI<sup>-</sup> anion exhibited the highest potential increase for H<sub>2</sub>O<sub>2</sub> oxidation due to the accumulation of cyclohexanone, it still possessed the highest H<sub>2</sub>O<sub>2</sub> oxidation current in the presence of cyclohexanone, which is greatly benefited from its coexistent hydrophilicity and hydrophobicity, originating from the two domains in the structure.

We used the same method to study the response of the hydrophobic interface (CP) to the anions. Without any cyclohexanone, unlike the hydrophilic Pt electrode, the different anions on the CP electrode showed similar H<sub>2</sub>O<sub>2</sub> oxidation current (Figure S14). It implies that the hydrophilicity or hydrophobicity of the anions does not affect much of the H<sub>2</sub>O<sub>2</sub> distribution on the hydrophobic CP electrode. The analysis of the potential difference at 10 mA/cm<sup>2</sup> with and without cyclohexanone also showed subtle differences among different anions, consistent with the trend of  $\epsilon$ -CL yield (Figure 2f). The hydrophobicity of the catalyst electrode is sufficient to drive the accumulation of cyclohexanone onto the interface such that the contribution from the anions can be negligible. Therefore, on the hydrophilic electrode, the hydrophilicity and hydrophobicity of the anions are the determining factor for the performance of electrochemical B–V oxidation, especially toward the realization of H<sub>2</sub>O<sub>2</sub> oxidation and cyclohexanone accumulation for B–V oxidation. Whereas on the hydrophobic electrode, the electrode can spontaneously accumulate cyclohexanone at the interface, and the performance might instead be governed by the intrinsic H<sub>2</sub>O<sub>2</sub> oxidation kinetics.

We further verified the aggregation effect of anions toward cyclohexanone by surface-enhanced infrared absorption spectroscopy (SEIRAS). A gold electrode was adopted to mimic the hydrophilic electrode and achieve a signal enhancement. Since the TFSI<sup>-</sup> anion begins to adsorb and accumulate on the electrode surface when the potential is above 0.7 V vs RHE (Figure S15), we could clearly resolve the S=O vibration peak in TFSI<sup>-</sup> (1350.4 cm<sup>-1</sup>) in the IR spectra (Figure 3a). This vibration peak showed a potential-dependent peak shift (Stark shift) of 0.7 cm<sup>-1</sup>/V, demonstrating the location of TFSI<sup>-</sup> near the vicinity of the electrode, likely on the outer Helmholtz plane. In coincidence, the C=O stretching peak of cyclohexanone (1700.8 cm<sup>-1</sup>) could also be observed under these applied potentials, suggesting that the accumulation of TFSI<sup>-</sup> through electrostatic interactions might drive the accumulation of cyclohexanone at the interface. In contrast, the hydrophilic anion SO<sub>4</sub><sup>2-</sup> also showed accumulation on the electrode surface by showing S=O vibration at 1230.8 cm<sup>-1</sup> with a Stark shift of 1.8 cm<sup>-1</sup>/V (Figure 3b). The different shifting direction of S=O vibrations from SO<sub>4</sub><sup>2-</sup> and TFSI<sup>-</sup> likely originated from their different overall dipole directions. However, the cyclo-

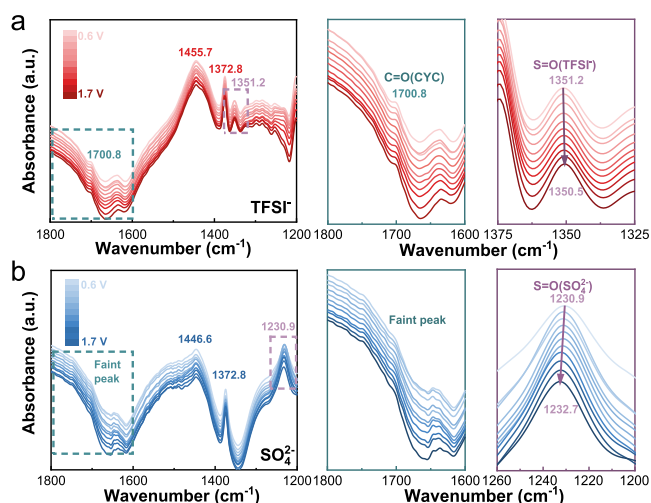


**Figure 3.** (a,b) ATR-SEIRAS spectra of the system in different electrolytes with TFSI<sup>−</sup> and SO<sub>4</sub><sup>2−</sup> anions upon polarization to different potentials. The magnified regions of cyclohexanone and anion vibrations are listed on the right.

hexanone signal is almost absent in these spectra, demonstrating much decreased cyclohexanone on the hydrophilic interface. It reflects that the hydrophilic anion is incapable of attracting hydrophobic cyclohexanone to the hydrophilic interface. This spectroscopic evidence can serve as another strong support for the previous studies on the  $\epsilon$ -CL yield and hydrophilicity/hydrophobicity of the anions.

#### Ion Concentration Effect on the Combined Direct/Indirect Oxidation Pathway

As TFSI<sup>−</sup> is both hydrophilic and hydrophobic, its interfacial behavior deserves attention, especially toward its accumulation

effect for cyclohexanone and H<sub>2</sub>O<sub>2</sub>. The ion concentration is a significant contributor to this accumulation effect, and consequently, we varied the TFSI<sup>−</sup> concentrations and examined the activity of electrochemical B–V oxidation on the hydrophilic Pt electrode. As the TFSI<sup>−</sup> concentration increased, the  $\epsilon$ -CL yield first increased and then decreased, with the optimal activity at a concentration of 0.1 M TFSI<sup>−</sup> (Figure 4a). We also measured the H<sub>2</sub>O<sub>2</sub> oxidation kinetics with and without cyclohexanone under different concentrations of TFSI<sup>−</sup> and quantified the potential differences to reach 10 mA/cm<sup>2</sup> (Figure 4b). The potential differences turned out to be scaled with the TFSI<sup>−</sup> concentrations, corresponding to the increased hydrophobicity. In fact, this is unexpected since in previous analysis this potential difference is a measure of interfacial hydrophobicity that mostly determines the B–V oxidation activity. However, this increased hydrophobicity did not lead to an increase in the  $\epsilon$ -CL yield but instead a steadily decreased  $\epsilon$ -CL yield. It suggested that this hydrophobicity is not a determining factor at high anion concentrations, which could be related to the observed decreased activities under more hydrophobic anion structures with aromatic rings or longer aliphatic chains. According to the H<sub>2</sub>O<sub>2</sub> oxidation kinetics without cyclohexanone, we resolved a gradual decrease in current upon adding more TFSI<sup>−</sup>, so we speculate that the H<sub>2</sub>O<sub>2</sub> oxidation might be hindered under enhanced hydrophobicity and thus dominated the activity trend. This may also reflect that the hydrophilic and hydrophobic domains of the TFSI<sup>−</sup> structure can act differently under different scenarios.

To illustrate the affinity of different concentrations of TFSI<sup>−</sup> to H<sub>2</sub>O<sub>2</sub> and cyclohexanone, we carried out MD simulation and statistically analyzed the distribution of H<sub>2</sub>O<sub>2</sub> and cyclohexanone at the reaction interface. We discovered that a significant portion of H<sub>2</sub>O<sub>2</sub> resides in the double layer close to

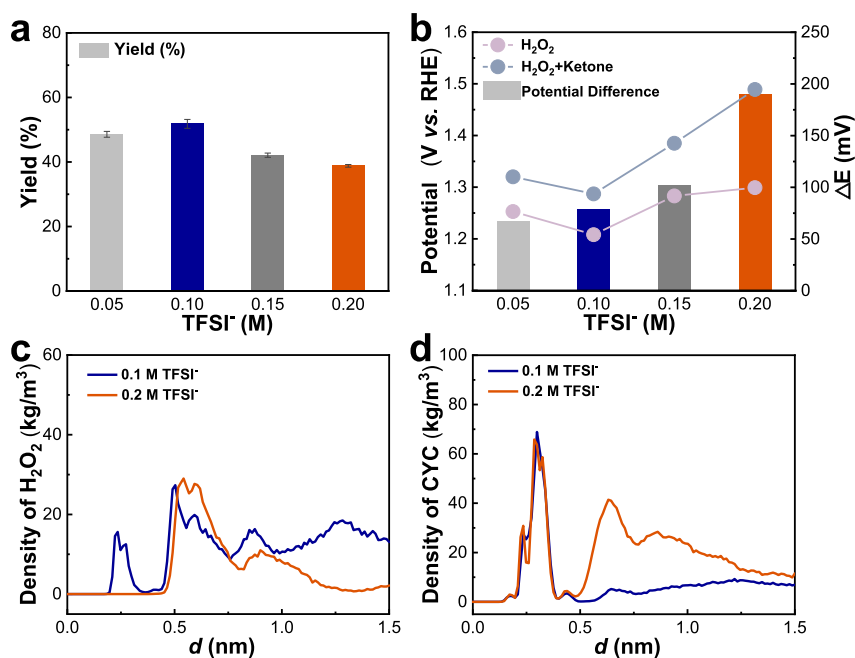


**Figure 4.** (a) Effect of the TFSI<sup>−</sup> concentration on  $\epsilon$ -CL yield on the Pt electrode. (b) Potentials and potential differences of H<sub>2</sub>O<sub>2</sub> oxidation at 10 mA/cm<sup>2</sup> with and without cyclohexanone under different TFSI<sup>−</sup> concentrations. (c,d) Simulated distribution of (c) H<sub>2</sub>O<sub>2</sub> and (d) cyclohexanone at the electrode/electrolyte interface under different TFSI<sup>−</sup> concentrations.

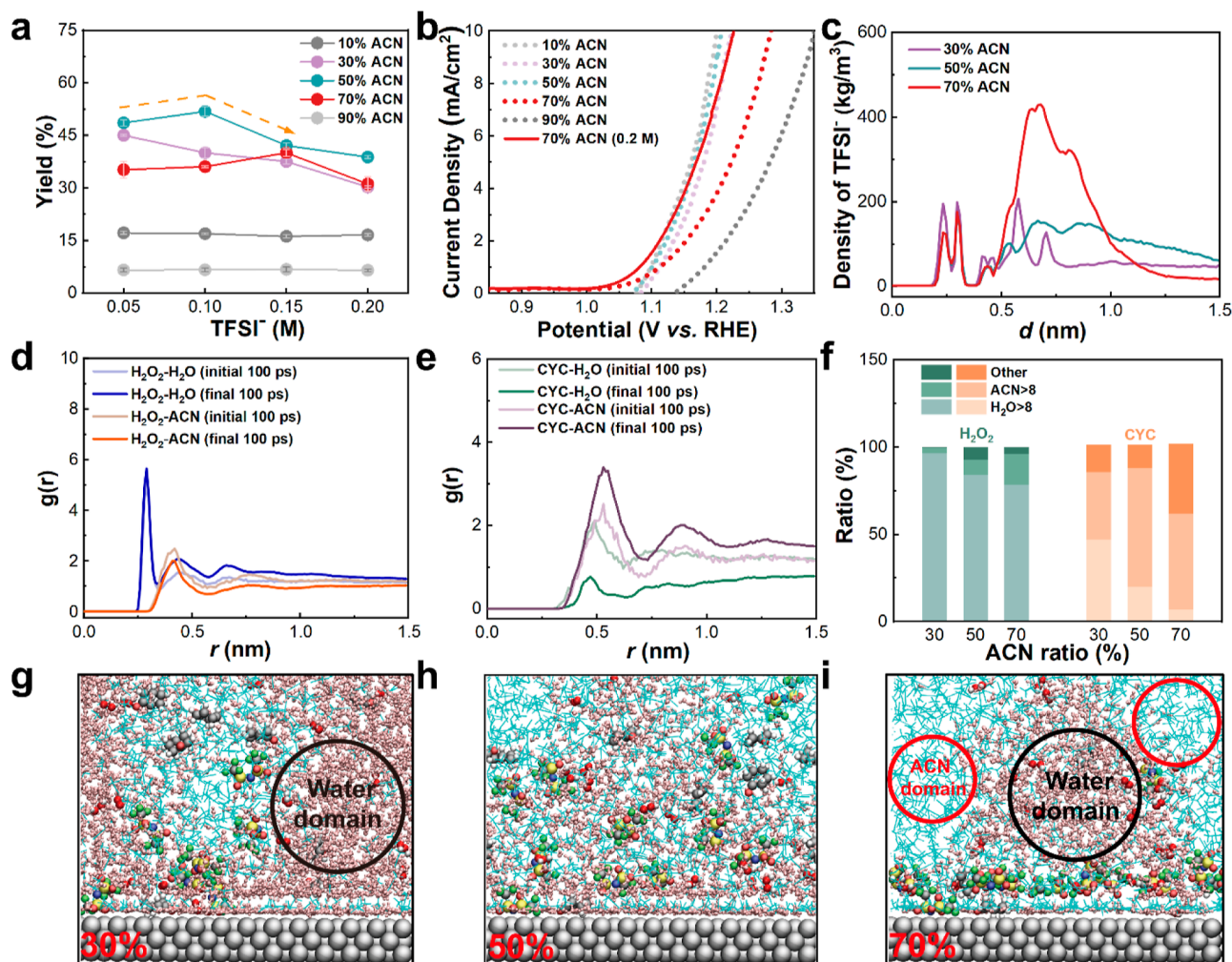


**Figure 5.** (a) Effect of the TFSI<sup>-</sup> concentration on  $\epsilon$ -CL yield under different acetonitrile/water ratios on the Pt electrode. (b) Polarization curves of the Pt electrode under 0.1 or 0.2 M TFSI<sup>-</sup> with different acetonitrile/water ratios. The scan rate is 10 mV/s. (c) Simulated distribution of TFSI<sup>-</sup> at the interface in the electrolyte with different acetonitrile/water ratios. (d,e) Affinity analysis of (d) H<sub>2</sub>O<sub>2</sub> and (e) cyclohexanone toward acetonitrile and water. (f) Distribution of acetonitrile and water in the vicinity of H<sub>2</sub>O<sub>2</sub> and cyclohexanone at the electrode/electrolyte interface. (g–i) Fast-shots of the simulated distribution of various species under different acetonitrile/water ratios.

the interface under 0.1 M TFSI<sup>-</sup>, while this fraction of H<sub>2</sub>O<sub>2</sub> almost disappears under 0.2 M TFSI<sup>-</sup> with mostly residing on the outside in the diffusion layer (Figure 4c). Due to the limited H<sub>2</sub>O<sub>2</sub> concentration and the distance of >0.2 nm away from the electrode, these H<sub>2</sub>O<sub>2</sub> are likely residing on the outer Helmholtz plane (OHP). However, considering the discrepant electrocatalytic activities of H<sub>2</sub>O<sub>2</sub> oxidation on different electrodes, the H<sub>2</sub>O<sub>2</sub> oxidation should take place in the manner of heterogeneous electrocatalysis with specific adsorption on the catalytic electrode (ca. direct oxidation). The lower concentration of H<sub>2</sub>O<sub>2</sub> within the double layer could lead to significantly reduced oxidation activity, which is consistent with the experimental observation of a higher H<sub>2</sub>O<sub>2</sub> oxidation overpotential under 0.2 M TFSI<sup>-</sup>. As for the cyclohexanone, varying the TFSI<sup>-</sup> concentration cast subtle changes on the distribution of cyclohexanone within the double layer but instead affect the distribution on the diffusion layer by accumulation of more cyclohexanone in 0.2 M TFSI<sup>-</sup> (Figure 4d). This distribution of cyclohexanone at the outside layer constantly varies via gradually diffusing the distribution peak into the bulk electrolyte upon extending the timescale of the simulation (Figure S16), which suggests the presence of a

high statistical variation for the analysis on the cyclohexanone distribution. Nevertheless, the cyclohexanone distribution within the double layer barely varies under different systems, indicating that the inner cyclohexanone is not a limiting factor for the activity, and the total concentration of cyclohexanone in the vicinity of the electrode is the actual influencing factor. This correlates well with the indirect oxidation mechanism between the •OOH radical and cyclohexanone that cyclohexanone does not need to be adsorbed on the electrode but needs to react with the reactive oxygen species before its annihilation and thus demands a high concentration near the interface.

Therefore, the electrochemical B–V oxidation of cyclohexanone requires both the direct oxidation of H<sub>2</sub>O<sub>2</sub> on the electrode that prefers H<sub>2</sub>O<sub>2</sub> accumulation within the double layer and the indirect oxidation between the reactive oxygen species and cyclohexanone that prefers cyclohexanone accumulation near the interface. This distribution is greatly affected by the total concentration of amphiphatic TFSI<sup>-</sup> anions. Upon increasing the concentration of TFSI<sup>-</sup> anions, we could resolve a steady increase of the TFSI<sup>-</sup> concentration on the OHP and diffusion layer (Figure S17). According to the

microscopic analysis around the TFSI<sup>-</sup> anion, it is relatively obvious that the hydrophobic domain of the TFSI<sup>-</sup> has high affinity to the acetonitrile solvent, such that the accumulation of TFSI<sup>-</sup> in the OHP attracts the acetonitrile molecules to the interface and creates a relatively more hydrophobic interface that expels the H<sub>2</sub>O<sub>2</sub> to the outer region. Consequently, direct H<sub>2</sub>O<sub>2</sub> oxidation could be drastically suppressed, leading to inferior activity.

### Amphipathic Anion for Dispersing the Mixed Solvent and Its Interaction Mechanism

In the above study, a mixed solvent of acetonitrile and water with a volume ratio of 1/1 was used to achieve the best  $\epsilon$ -CL yield. We found that the mixed solvent ratio is another key parameter that affects the catalytic activity. Either decreasing or increasing the proportion of acetonitrile negatively impacted on the  $\epsilon$ -CL yield under various TFSI<sup>-</sup> concentrations (Figure 5a). As we mentioned earlier, an optimal TFSI<sup>-</sup> concentration is required for the maximal yield of  $\epsilon$ -CL. Another interesting phenomenon is that the optimal TFSI<sup>-</sup> concentration is higher under larger proportions of acetonitrile (30%, 0.05 M; 50%, 0.10 M; and 70%, 0.15 M) (Figure 5a). This is rather counterintuitive, since more acetonitrile should generate a more hydrophobic interface, which should require fewer TFSI<sup>-</sup> anions to create the hydrophobic environment for cyclohexanone accumulation and not to exclude the interfacial H<sub>2</sub>O<sub>2</sub> for direct oxidation. Accordingly, we render that the TFSI<sup>-</sup> anion is not acting on itself to regulate the interfacial structure but instead affects the local solvent environment that influences the distribution of H<sub>2</sub>O<sub>2</sub> and cyclohexanone near the interface.

We first conducted an analysis of the electrochemical H<sub>2</sub>O<sub>2</sub> oxidation kinetics on various acetonitrile/water ratios. As the proportion of acetonitrile becomes larger, the H<sub>2</sub>O<sub>2</sub> oxidation current decreases, especially then the proportion of acetonitrile exceeds 70% (Figure 5b). This is consistent with the expectation that more acetonitrile molecules create a more hydrophobic interface that expels the interfacial H<sub>2</sub>O<sub>2</sub>. However, when we further increased the TFSI<sup>-</sup> concentration to 0.2 M, the H<sub>2</sub>O<sub>2</sub> oxidation current drastically improved rather than decreasing as in the case of the aforementioned 1/1 acetonitrile/water electrolyte. It implied that the TFSI<sup>-</sup> anion is not simply modulating the interfacial distribution of different species by itself but instead by another unexplored mechanism.

To glean the underlying influencing mechanism of anions, we performed MD simulations on the electrolyte systems with different acetonitrile/water ratios. Specifically, the 30/50/70% acetonitrile electrolytes were studied. We first examined the affinity of TFSI<sup>-</sup> for the two solvent molecules (acetonitrile and water). As the acetonitrile ratio increases, the density of TFSI<sup>-</sup> anions at the OHP is not much affected much, but the number of those further away is significantly increased (Figure 5c). It suggests that TFSI<sup>-</sup> has a higher affinity for acetonitrile than for water molecules. This could be confirmed by the microscopic analysis on the shot of MD simulation that TFSI<sup>-</sup> tends to gather acetonitrile in the surroundings. It might reflect that the amphipathic TFSI<sup>-</sup> does not directly affect the H<sub>2</sub>O<sub>2</sub> and cyclohexanone but through the solvent distribution in the local structures indirectly affects the substrate distribution.

Subsequently, we carried out affinity analysis between the solvent and substrate in the system with 50% acetonitrile. Before and after the reaction system stabilized, H<sub>2</sub>O<sub>2</sub> showed a clear trend of migrating toward the water area and away from

the acetonitrile area (Figure 5d). It means that H<sub>2</sub>O<sub>2</sub> is more hydrophilic and more likely stays in the vicinity of water rather than acetonitrile or at the junction of the two solvents. When the acetonitrile content is low (30%), water dominates the space, and the migration of H<sub>2</sub>O<sub>2</sub> is not obvious. When the acetonitrile content is high (70%), acetonitrile dominates the space, and water molecules easily form domains, to which the migration of H<sub>2</sub>O<sub>2</sub> can be clearly resolved (Figure S18). In comparison, cyclohexanone showed a completely opposite trend, with a tendency to migrate toward acetonitrile and away from water (Figure 5e). The lower the acetonitrile content, the more obvious the migration of cyclohexanone (Figure S19). Unlike H<sub>2</sub>O<sub>2</sub>, there is no significant difference in the distance between water/acetonitrile and cyclohexanone, which indicates that cyclohexanone more likely exists near the interfacial region of water and acetonitrile. In other words, the more dispersed the solvent, the more preferred is the distribution of cyclohexanone.

We then performed statistical analysis on the local distribution of various species around the two substrates, H<sub>2</sub>O<sub>2</sub> and cyclohexanone, near the reaction interface (Figure 5f). As the proportion of acetonitrile increases, both H<sub>2</sub>O<sub>2</sub> and cyclohexanone show the trend of decreasing proportions in the water-rich area and increasing proportions in the acetonitrile-rich area. When the acetonitrile content is 50%, its proportion at the junction of the acetonitrile/water zone reaches the highest, which could be beneficial for the reaction since the generated  $\bullet$ OOH radical must be efficiently trapped by an acetonitrile molecule to form the reactive species. In contrast, despite the similarly decreased proportion in the water area, cyclohexanone is not increasing its proportion in the acetonitrile area but instead resides at the junction area at a high acetonitrile content of 70%. This could be related to the amphipathic nature of cyclohexanone and the formation of acetonitrile domains at high acetonitrile content, which will be discussed later.

These results inspired us to carry out a detailed analysis of the microscopic structure at the interface via MD simulation. When the acetonitrile content is 30%, the electrode surface is mainly composed of water and a trace amount of acetonitrile. In the vicinity of the interface, we could clearly observe the formation of water-rich and acetonitrile-rich domains that separate the electrolyte. H<sub>2</sub>O<sub>2</sub> mostly resides in the water-rich domains, suggesting its hydrophilicity. Since the double layer consists of a large content of water molecules, the accumulation of H<sub>2</sub>O<sub>2</sub> at the interface could be facile for accelerating the oxidation kinetics. However, the acetonitrile domain tends to stay away from the interface, thus hindering its potential reaction with the reactive oxygen species upon H<sub>2</sub>O<sub>2</sub> oxidation. In addition, cyclohexanone mostly exists in the acetonitrile-rich domain or at the junction area, which lowers its possibility of reacting with the oxygen species (Figure 5g). As a consequence, the limiting step of the reaction is the indirect oxidation of cyclohexanone, including the reaction between acetonitrile and  $\bullet$ OOH radicals. When the acetonitrile content reaches 50%, due to the amphipathic TFSI<sup>-</sup> anion and even acetonitrile/water ratios, the two solvents at the interfacial region are well dispersed. This solvent state is conducive not only to H<sub>2</sub>O<sub>2</sub> enrichment but also to the approach of cyclohexanone to the surface (Figure 5h). As a result, the two subreactions of direct H<sub>2</sub>O<sub>2</sub> oxidation and indirect oxidation of cyclohexanone can be well coupled to achieve the efficient electrochemical B–V oxidation. When the



acetonitrile content is 70%, a large number of acetonitrile domains exist, accompanied by the segregation of water-rich domains. In this case, a large number of TFSI<sup>-</sup> anions are utilized to stabilize the electrochemical interface, whereas very few numbers of TFSI<sup>-</sup> anions can be utilized to break the domains to disperse the solvent. This is highly consistent with the higher TFSI<sup>-</sup> concentrations demanded to reach a higher  $\epsilon$ -CL yield under a high acetonitrile proportion. In this scenario, it is more facile to enrich cyclohexanone at the interface while H<sub>2</sub>O<sub>2</sub> mainly exists in the distant water domains that decelerates its oxidation (Figure S1). Thus, the limiting step is the direct oxidation of H<sub>2</sub>O<sub>2</sub> at the interface. In summary, only the TFSI<sup>-</sup> concentration matches the acetonitrile ratio, such that acetonitrile and water can be well dispersed. The dispersion of the two solvent molecules is highly critical to the effective enrichment of H<sub>2</sub>O<sub>2</sub> and cyclohexanone at the interface for coupled direct H<sub>2</sub>O<sub>2</sub> oxidation and indirect cyclohexanone oxidation toward efficient B–V oxidation.

## CONCLUSION

In this work, we propose an efficient route of electrochemical B–V oxidation of cyclohexanone into  $\epsilon$ -CL by adjusting the local distribution of active species at the electrode/electrolyte interface. This adjustment was achieved by tuning the types of anions in the reaction system, thereby realizing a substantial increase in the  $\epsilon$ -CL yield from 29.54% of SO<sub>4</sub><sup>2-</sup> to 52.10% of TFSI<sup>-</sup>. We attributed the improvement in the  $\epsilon$ -CL yield to the amphipathic property of the TFSI<sup>-</sup> anion with both hydrophilic S=O domains and hydrophobic CF<sub>3</sub> domains, which can distribute the hydrophilic H<sub>2</sub>O<sub>2</sub> and the hydrophobic cyclohexanone appropriately at the interface. Generally, these amphipathic anions outperformed other anions that are more hydrophilic and more hydrophobic, but this trend is highly dependent on the electrode hydrophilicity/hydrophobicity. The hydrophilic electrode is limited by accumulation of cyclohexanone near the interface, such that the anion is a great contributor to the  $\epsilon$ -CL yield whereas the hydrophobic electrode is sufficient to drive the spontaneous adsorption of cyclohexanone and in turn limited by H<sub>2</sub>O<sub>2</sub> oxidation, so that the anion is negligibly affecting the performance. Steady-state electrochemical kinetics, in situ spectroscopy, and MD simulation results show that the solvent distribution has a great effect and the anions mostly act on the solvent molecules to evenly distribute them at the electrode/electrolyte interface. The water/acetonitrile electrolyte system facily forms domains that disfavor the interfacial distribution of activity species, and the amphipathic TFSI<sup>-</sup> anions act to break the domains, allowing the accumulation of H<sub>2</sub>O<sub>2</sub> at the electrode surface and the accumulation of cyclohexanone near the interface for promptly reacting with the active oxygen species. Through the efficient manipulation of local molecular distribution, we can achieve the efficient electrochemical B–V oxidation coupled with cathodic hydrogen evolution toward the sustainable and green electrified production of biodegradable polymer precursors. This work also emphasizes the significance of tuning the ionic environment for complicated electrosynthesis systems, which may open up new opportunities for optimizing the performance or finding new reactivities.

## EXPERIMENTAL SECTION

### Catalyst Electrode Preparation

Carbon paper, platinum sheet, stainless-steel mesh, and graphite plate (1 cm × 1 cm × 0.1 cm) were ultrasonically washed with deionized water and ethanol to remove surface contaminants. The titanium mesh was thoroughly polished to remove the surface oxide layer before being subjected to the same treatment. The electrochemical workstation (CHI 660E, Shanghai CH Instruments Co., China) was used for the potential control.

### Electrochemical Measurements

The electrochemical measurements were performed on a CHI660E workstation using a standard 5 mL electrochemical cell with a three-electrode system. The as-prepared electrodes directly served as the working electrode. A graphite rod and a Ag/AgCl electrode in saturated KCl were used as the counter electrode and the reference electrode, respectively. All of the measured potentials in our work were converted to a reversible hydrogen electrode (RHE) scale using the Nernst equation.

$$E(\text{RHE}) = E(\text{Ag/AgCl}) + 0.197 + 0.0591 \times \text{pH} \quad (1)$$

The kinetics study was examined by polarization curves under a scan rate of 10 mV/s, corrected with an 80% *i*R-compensation. In the ketone electrolysis experiment, all reactions took place in a 5 mL electrolytic cell with a stirring speed of 600 rpm and a constant current of 10 mA. The conventional experimental conditions are as follows: 60 mM cyclohexanone, 360 mM H<sub>2</sub>O<sub>2</sub>, 0.1 M salt + acetonitrile/water = *x*/*y* (*x*/*y* = 9:1, 7:3, 5:5, 3:7, and 1:9) for 3 h. In the substrate expansion experiment, in order to fully convert the substrate, we changed the reaction conditions to 60 mM ketone, 720 mM H<sub>2</sub>O<sub>2</sub>, 0.1 M LiTFSI, and acetonitrile/water = 1:1 for 6 h. All experiments were conducted at a room temperature of 25 °C.

### Electrolysis Product Analysis

The products were analyzed by a nuclear magnetic resonance (NMR, Bruker 400 MHz Avance III HD) spectrometer and gas chromatography–mass spectrometry (GC–MS) technology. The  $\epsilon$ -CL product was quantified by <sup>1</sup>H NMR with fumaric acid as the internal standard. The standard method includes adding 100  $\mu$ L of the electrolyte into a 400  $\mu$ L D<sub>2</sub>O solution with 100  $\mu$ L of 0.01 M fumaric acid. The number of moles of the product (*n* <sub>$\epsilon$ -CL</sub>) was calculated by using the following equation.

$$n_{\epsilon\text{-CL}} = \frac{A_{\epsilon\text{-CL}} \times N_{\text{fumaric acid}}}{A_{\text{fumaric acid}} \times N_{\epsilon\text{-CL}}} \times n_{\text{fumaric acid}} \quad (2)$$

where *A* <sub>$\epsilon$ -CL</sub> is the integral area of the  $\epsilon$ -CL peak (2.60 ppm) in the NMR spectrum (Figure S5), which corresponds to two protons, and *N* <sub>$\epsilon$ -CL</sub> is the corresponding H number (*N* <sub>$\epsilon$ -CL</sub> = 2). *A*<sub>fumaric acid</sub> is the integral area of the fumaric acid peak (6.70 ppm), and *N*<sub>fumaric acid</sub> is the corresponding H number (*N*<sub>fumaric acid</sub> = 2) of the fumaric acid peak.

### Gas Chromatography–Mass Spectrometry

GC–MS analysis was performed on an Agilent (Little Falls, DE, USA) gas chromatograph 8890 equipped with an inert 5977B mass selective detector with an electron impact (EI) ionization chamber. An Agilent HP-5 capillary column (15 m × 250  $\mu$ m × 0.25  $\mu$ m) was used for the separation of analytes. The initial GC oven temperature was set at 40 °C and ramped at 40 °C/min to 250 °C and held for 5 min. A split injection (split ratio, 20:1) and an injector temperature of 250 °C were employed. Helium was used as the carrier gas at a constant flow rate of 1 mL/min. The pretreatment before injection is as follows: 1 mL of reaction solution, 1 × 3 mL of methylene chloride, separate through a separatory funnel, add sodium sulfate to dry the product, and filter through a 0.45  $\mu$ m filter membrane.

### Acetamide Analysis

Acetamide content was analyzed by high-performance liquid chromatography (HPLC, Waters 2487). For each HPLC measurement, a quantitative electrolyte solution was sampled from the

electrochemical cell, and the aqueous phase was collected after extraction with diethyl ether. It was then diluted with 10 mM H<sub>2</sub>SO<sub>4</sub> solution (to adjust the pH below 7.0), and 10  $\mu$ L of the resulting mixture was injected into a BioRad Aminex 87H column. 5 mM H<sub>2</sub>SO<sub>4</sub> solution was used as the mobile phase, isocratic mode, with a constant flow rate (0.6 mL·min<sup>-1</sup>) and a column temperature of 65 °C. The acetamide product was identified by comparing the retention times of HPLC elution peaks with individual standard sample solutions. The yield was calculated by the product concentration based on the calibration curve using standard solutions.

### In Situ ATR-SEIRAS Analysis

Due to the similar surface properties of Au and Pt, we directly used the Au disk electrode ( $\Phi = 10$  mm) as our working electrode. The ATR-SEIRAS spectra were collected with a Nicolet iS20 FTIR spectrometer (Nicolet iS20 FTIR, Thermo Scientific) with a built-in MCT detector and an in situ IR optical accessory (SPEC-I, Shanghai Yuanfang Tech. Co., Ltd., China). The Au-coated Si prism was used as the working electrode, with the Ag/AgCl electrode and the Pt foil as the reference and counter electrodes, respectively. Potentiodynamic measurement was conducted in the N<sub>2</sub>-saturated atmosphere, and  $\sim 10$  sccm N<sub>2</sub> flow was kept bubbling through the spectroelectrochemical cell and infrared spectrometer. ATR spectra were acquired at a resolution of 4 cm<sup>-1</sup> with unpolarized IR radiation at an incidence angle of ca. 60°. All spectra were converted to the absorbance unit as  $\log(I/I_0)$ , where  $I$  and  $I_0$  represent the signal intensities of the reflected radiation of the sample and reference spectra. The electrochemical workstation (CHI 660E, Shanghai CH Instruments Co., China) was utilized for the potential control.

### Bulk MD Simulations

Classical MD simulations were conducted by using the GROMACS program and the OPLS-AA force field. We used a six-site ACN model and a four-site water model (OPC). The structural files of hydrogen peroxide, cyclohexanone, and [TFSE<sup>-</sup>] were obtained from the ATB database, and the RESP atomic charges of each molecule were calculated. The simulations were performed in the NPT ensemble for 2 ns, and both temperature coupling (300 K) and pressure coupling (1 atm) were performed using the Berendsen method with a relaxation constant of 1 ps. The time step was set to 1 fs, and the system structure was recorded at intervals of 1 ps. Periodic boundary conditions were applied in the xyz directions. The configuration of all boxes is provided in Table S2. Acetonitrile molecules and water molecules were added to a large box and compressed to a stable density during the simulation process in the NPT ensemble. Energy minimization was performed before the formal simulation began. Long-range electrostatic interactions and van der Waals interactions were calculated using the fast smooth particle mesh Ewald (SPME) method and cutoff method, respectively, and the cutoff distance of both was set to 2 nm. The quality density of the entire system during the simulation process was calculated by using the algorithm integrated in the GROMACS program.

### MD Simulations of the Electrode–Electrolyte Interface

The simulation system consists of two Pt electrodes with a spacing of 10 nm and an electrolyte between the electrodes (Figure S20). 3D periodic boundary conditions are used in the xyz directions, and a vacuum layer with a thickness of 2 nm is set in the  $z$  direction to prevent mutual influence between the two electrodes. The spatial position of electrode atoms is fixed during the simulation process, and the electrode atoms in contact with the electrolyte are set with an atomic charge of  $\pm 0.025$  e. More details about the simulation system are shown in Figures S20 and S21 and Table S3. The simulations are performed in the NVT ensemble for 10 ns. The setting of temperature coupling, the calculation of long-range electrostatic interactions, and van der Waals interactions is the same as in the bulk simulations. The trajectory of the last 5 ns of the simulations to analyze the distribution of each component is chosen, unless otherwise marked. VMD software is used to generate snapshots of simulated systems.

## ■ ASSOCIATED CONTENT

### Supporting Information

The Supporting Information is available free of charge at <https://pubs.acs.org/doi/10.1021/jacsau.4c00585>.

Additional product and yield analysis; catalyst analysis; and experimental and computational results to support the proposed catalytic mechanism (PDF)

## ■ AUTHOR INFORMATION

### Corresponding Authors

**Cheng Lian** – State Key Laboratory of Chemical Engineering, School of Chemistry and Molecular Engineering, East China University of Science and Technology, Shanghai 200237, China; [orcid.org/0000-0002-9016-832X](https://orcid.org/0000-0002-9016-832X); Email: [liancheng@ecust.edu.cn](mailto:liancheng@ecust.edu.cn)

**Ming Gong** – Department of Chemistry, Shanghai Key Laboratory of Molecular Catalysis and Innovative Materials and Collaborative Innovation Center of Chemistry for Energy Materials (iChEM), Fudan University, Shanghai 200438, China; [orcid.org/0000-0002-1584-1211](https://orcid.org/0000-0002-1584-1211); Email: [gongm@fudan.edu.cn](mailto:gongm@fudan.edu.cn)

### Authors

**Shuangshuang Cha** – Department of Chemistry, Shanghai Key Laboratory of Molecular Catalysis and Innovative Materials and Collaborative Innovation Center of Chemistry for Energy Materials (iChEM), Fudan University, Shanghai 200438, China

**Yuxin Chen** – State Key Laboratory of Chemical Engineering, School of Chemistry and Molecular Engineering, East China University of Science and Technology, Shanghai 200237, China

**Wei Du** – Department of Chemistry, Shanghai Key Laboratory of Molecular Catalysis and Innovative Materials and Collaborative Innovation Center of Chemistry for Energy Materials (iChEM), Fudan University, Shanghai 200438, China

**Jianxiang Wu** – Department of Chemistry, Shanghai Key Laboratory of Molecular Catalysis and Innovative Materials and Collaborative Innovation Center of Chemistry for Energy Materials (iChEM), Fudan University, Shanghai 200438, China; College of Environmental and Chemical Engineering, Shanghai University of Electric Power, Shanghai 200090, China

**Ran Wang** – Department of Chemistry, Shanghai Key Laboratory of Molecular Catalysis and Innovative Materials and Collaborative Innovation Center of Chemistry for Energy Materials (iChEM), Fudan University, Shanghai 200438, China

**Tao Jiang** – Department of Chemistry, Shanghai Key Laboratory of Molecular Catalysis and Innovative Materials and Collaborative Innovation Center of Chemistry for Energy Materials (iChEM), Fudan University, Shanghai 200438, China

**Xuejing Yang** – National Engineering Laboratory for Industrial Wastewater Treatment, East China University of Science and Technology, Shanghai 200237, China; [orcid.org/0000-0001-5144-4400](https://orcid.org/0000-0001-5144-4400)

**Honglai Liu** – State Key Laboratory of Chemical Engineering, School of Chemistry and Molecular Engineering, East China

University of Science and Technology, Shanghai 200237, China; [orcid.org/0000-0002-5682-2295](https://orcid.org/0000-0002-5682-2295)

Complete contact information is available at:  
<https://pubs.acs.org/10.1021/jacsau.4c00585>

### Author Contributions

<sup>†</sup>S.C. and Y.C. contributed equally. Cheng Lian and Ming Gong conceived the idea, designed the research project, and cowrote the manuscript. Shuangshuang Cha performed the experiments, collected and analyzed the data, and cowrote the manuscript. Yuxin Chen contributed to the computational results and cowrote the manuscript. Wei Du, Jianxiang Wu, Ran Wang, Tao Jiang, Xuejing Yang, and Honglai Liu helped to analyze the data and write the manuscript. All the authors discussed the results and commented on the paper.

### Notes

The authors declare no competing financial interest.

### ACKNOWLEDGMENTS

This work was financially supported by National Natural Science Foundation of China (22172036), the Shanghai Technology Innovation Program (Carbon-Neutral Program, 21DZ1207800), and the Fundamental Research Funds for the Central Universities (20720220011).

### REFERENCES

- (1) Shen, M.; Song, B.; Zeng, G.; Zhang, Y.; Huang, W.; Wen, X.; Tang, W. Are biodegradable plastics a promising solution to solve the global plastic pollution? *Environ. Pollut.* **2020**, *263*, 114469.
- (2) Chen, L.; Liu, Y.; Chi, J.; Xiong, W.; Liu, P.; Hao, F. A highly efficient bifunctional copper catalyst for Baeyer-Villiger oxidation of cyclohexanone: Two different active centers and the reaction path investigation. *Appl. Surf. Sci.* **2023**, *638*, 158045.
- (3) Stegmann, P.; Daioglou, V.; Londo, M.; van Vuuren, D. P.; Junginger, M. Plastic futures and their CO<sub>2</sub> emissions. *Nature* **2022**, *612* (7939), 272–276.
- (4) Kwon, D. Three ways to solve the plastics pollution crisis. *Nature* **2023**, *616* (7956), 234–237.
- (5) Aresta, M.; Dibenedetto, A.; Angelini, A. Catalysis for the valorization of exhaust carbon: from CO<sub>2</sub> to chemicals, materials, and fuels. Technological use of CO<sub>2</sub>. *Chem. Rev.* **2014**, *114* (3), 1709–1742.
- (6) Thakur, M.; Majid, I.; Hussain, S.; Nanda, V. Poly( $\epsilon$ -caprolactone): A potential polymer for biodegradable food packaging applications. *Technol. Sci.* **2021**, *34* (8), 449–461.
- (7) Haider, T. P.; Völker, C.; Kramm, J.; Landfester, K.; Wurm, F. R. Plastics of the future? The impact of biodegradable polymers on the environment and on society. *Angew. Chem., Int. Ed.* **2019**, *58* (1), 50–62.
- (8) Bińczak, J.; Szelwicka, A.; Siewniak, A.; Dziuba, K.; Chrobok, A. Oxidation of Cyclohexanone with Peracids-A Straight Path to the Synthesis of  $\epsilon$ -Caprolactone Oligomers. *Materials* **2022**, *15* (19), 6608.
- (9) Pawar, R.; Pathan, A.; Nagaraj, S.; Kapare, H.; Giram, P.; Wavhale, R. Polycaprolactone and its derivatives for drug delivery. *Adv. Technol.* **2023**, *34* (10), 3296–3316.
- (10) Hong, B. J.; Chipre, A. J.; Nguyen, S. T. Acid-degradable polymer-caged lipoplex (PCL) platform for siRNA delivery: facile cellular triggered release of siRNA. *J. Am. Chem. Soc.* **2013**, *135* (47), 17655–17658.
- (11) Leisch, H.; Morley, K.; Lau, P. C. Baeyer-Villiger mono-oxygenases: more than just green chemistry. *Chem. Rev.* **2011**, *111* (7), 4165–4222.
- (12) Ten Brink, G.-J.; Arends, I.; Sheldon, R. The Baeyer-Villiger reaction: New developments toward greener procedures. *Chem. Rev.* **2004**, *104* (9), 4105–4124.
- (13) Jeong, E.-Y.; Ansari, M. B.; Park, S.-E. Aerobic Baeyer-Villiger oxidation of cyclic ketones over metalloporphyrins bridged periodic mesoporous organosilica. *ACS Catal.* **2011**, *1* (8), 855–863.
- (14) Maalouf, J. H.; Jin, K.; Yang, D.; Limaye, A. M.; Manthiram, K. Kinetic analysis of electrochemical lactonization of ketones using water as the oxygen atom source. *ACS Catal.* **2020**, *10* (10), 5750–5756.
- (15) Cai, Z.; Liu, D.; Huang, J.; Feng, J.; Wang, H.; Yang, G.; Peng, F.; Cao, Y.; Yu, H. Solvent-free production of  $\epsilon$ -caprolactone from oxidation of cyclohexanone catalyzed by nitrogen-doped carbon nanotubes. *Ind. Eng. Chem. Res.* **2022**, *61* (5), 2037–2044.
- (16) Lambert, A.; Elings, J.; Macquarrie, D. J.; Carr, G.; Clark, J. H. The Baeyer-Villiger oxidation of ketones using HMS supported peroxycarboxylic acids. *Synlett* **2000**, *2000* (07), 1052–1054.
- (17) Yoshida, A.; Yoshimura, M.; Uehara, K.; Hikichi, S.; Mizuno, N. Formation of S-Shaped Disilicoicosatungstate and Efficient Baeyer-Villiger Oxidation with Hydrogen Peroxide. *Angew. Chem., Int. Ed.* **2006**, *45* (12), 1990–1994.
- (18) Ma, Q.; Xing, W.; Xu, J.; Peng, X. Baeyer-Villiger oxidation of cyclic ketones with aqueous hydrogen peroxide catalyzed by transition metal oxides. *Catal. Commun.* **2014**, *53*, 5–8.
- (19) Uyanik, M.; Ishihara, K. Baeyer-Villiger oxidation using hydrogen peroxide. *ACS Catal.* **2013**, *3* (4), 513–520.
- (20) Ma, Q.; Xue, Y.; Guo, J.; Peng, X. The Baeyer-Villiger Oxidation of Cycloketones Using Hydrogen Peroxide as an Oxidant. *Catalysts* **2022**, *13* (1), 21.
- (21) Corma, A.; Nemeth, L. T.; Renz, M.; Valencia, S. Sn-zeolite beta as a heterogeneous chemoselective catalyst for Baeyer-Villiger oxidations. *Nature* **2001**, *412* (6845), 423–425.
- (22) Basso, A.; Serban, S. Industrial applications of immobilized enzymes-A review. *Mol. Catal.* **2019**, *479*, 110607.
- (23) Wu, S.; Snajdrova, R.; Moore, J. C.; Baldenius, K.; Bornscheuer, U. T. Biocatalysis: enzymatic synthesis for industrial applications. *Angew. Chem., Int. Ed.* **2021**, *60* (1), 88–119.
- (24) Füst, M. J. L. J.; Gran-Scheuch, A.; Aalbers, F. S.; Fraaije, M. W. Baeyer-Villiger mono-oxygenases: tunable oxidative biocatalysts. *ACS Catal.* **2019**, *9* (12), 11207–11241.
- (25) Mansouri, H. R.; Gracia Carmona, O.; Jodlbauer, J.; Schweiger, L.; Fink, M. J.; Breslmayr, E.; Laurent, C.; Feroz, S.; P Goncalves, L. C.; Rial, D. V.; et al. Mutations Increasing Cofactor Affinity, Improve Stability and Activity of a Baeyer-Villiger Mono-oxygenase. *ACS Catal.* **2022**, *12* (19), 11761–11766.
- (26) Szelwicka, A.; Wolny, A.; Grymel, M.; Jurczyk, S.; Boncel, S.; Chrobok, A. Chemo-enzymatic Baeyer-Villiger oxidation facilitated with lipases immobilized in the supported ionic liquid phase. *Materials* **2021**, *14* (13), 3443.
- (27) Wang, R.; Li, C.; Wu, J.; Du, W.; Jiang, T.; Yang, Y.; Yang, X.; Gong, M. Coordination-Promoted Bio-Catechol Electro-Reforming toward Sustainable Polymer Production. *J. Am. Chem. Soc.* **2023**, *145* (33), 18516–18528.
- (28) Herman, A.; Mathias, J.-L.; Neumann, R. Electrochemical Formation and Activation of Hydrogen Peroxide from Water on Fluorinated Tin Oxide for Baeyer-Villiger Oxidation Reactions. *ACS Catal.* **2022**, *12* (7), 4149–4155.
- (29) Mu, Y.; Chen, B.; Zhang, H.; Fei, M.; Liu, T.; Mehta, N.; Wang, D. Z.; Miller, A. J.; Diaconescu, P. L.; Wang, D. Highly Selective Electrochemical Baeyer-Villiger Oxidation through Oxygen Atom Transfer from Water. *J. Am. Chem. Soc.* **2024**, *146* (19), 13438–13444.
- (30) Ling, C.; Liu, X.; Li, H.; Wang, X.; Gu, H.; Wei, K.; Li, M.; Shi, Y.; Ben, H.; Zhan, G.; et al. Atomic-layered Cu<sub>5</sub> nanoclusters on FeS<sub>2</sub> with dual catalytic sites for efficient and selective H<sub>2</sub>O<sub>2</sub> activation. *Angew. Chem., Int. Ed.* **2022**, *61* (21), No. e202200670.
- (31) Yang, C.; Shang, S.; Lin, L.; Wang, P.; Ye, Z.; Wang, Y.; Shih, K.; Sun, L.; Li, X.-y. Electro-driven cycling Fenton catalysis through two-dimensional electroresponsive metal-organic frameworks for

water purification. *Nat. Water* **2024**, DOI: 10.1038/s44221-024-00262-1.

(32) Yang, W.; Zhu, M.; Li, W.; Liu, G.; Zeng, E. Y. Surface-catalyzed electro-Fenton with flexible nanocatalyst for removal of plasticizers from secondary wastewater effluent. *J. Hazard. Mater.* **2022**, *435*, 129023.

(33) Wang, J.; Hou, K.-P.; Wen, Y.; Liu, H.; Wang, H.; Chakarawet, K.; Gong, M.; Yang, X. Interlayer structure manipulation of iron oxychloride by potassium cation intercalation to steer H<sub>2</sub>O<sub>2</sub> activation pathway. *J. Am. Chem. Soc.* **2022**, *144* (10), 4294–4299.

(34) Tan, Z.; Cao, P.; Chen, S.; Yu, H.; Su, Y.; Quan, X. Highly efficient electrocatalysis of oxygen to hydroxyl radical by FeN<sub>2</sub>O<sub>2</sub> single-atom catalyst for refractory organic pollutant removal. *Appl. Catal., B* **2024**, *355*, 124170.

(35) Yu, D.; Xu, L.; Fu, K.; Liu, X.; Wang, S.; Wu, M.; Lu, W.; Lv, C.; Luo, J. Electronic structure modulation of iron sites with fluorine coordination enables ultra-effective H<sub>2</sub>O<sub>2</sub> activation. *Nat. Commun.* **2024**, *15* (1), 2241.

(36) Dorchies, F.; Serva, A.; Crevel, D.; De Freitas, J.; Kostopoulos, N.; Robert, M.; Sel, O.; Salanne, M.; Grimaud, A. Controlling the hydrophilicity of the electrochemical interface to modulate the oxygen-atom transfer in electrocatalytic epoxidation reactions. *J. Am. Chem. Soc.* **2022**, *144* (49), 22734–22746.

(37) Dubouis, N.; Serva, A.; Berthin, R.; Jeanmairet, G.; Porcheron, B.; Salager, E.; Salanne, M.; Grimaud, A. Tuning water reduction through controlled nanoconfinement within an organic liquid matrix. *Nat. Catal.* **2020**, *3* (8), 656–663.

(38) Jimenezsanchidrian, C.; Hidalgo, J. M.; Llamas, R.; Ruiz, J. R. Baeyer-Villiger oxidation of cyclohexanone with hydrogen peroxide/benzonitrile over hydrotalcites as catalysts. *Appl. Catal., A* **2006**, *312*, 86–94.

(39) Sever, R. R.; Root, T. W. Computational study of tin-catalyzed Baeyer-Villiger reaction pathways using hydrogen peroxide as oxidant. *J. Phys. Chem. B* **2003**, *107* (39), 10848–10862.

(40) Deng, F.; Olvera-Vargas, H.; Zhou, M.; Qiu, S.; Sirés, I.; Brillas, E. Critical Review on the Mechanisms of Fe<sup>2+</sup> Regeneration in the Electro-Fenton Process: Fundamentals and Boosting Strategies. *Chem. Rev.* **2023**, *123* (8), 4635–4662.

(41) Liao, Q.; Sun, Q.; Xu, H.; Wang, Y.; Xu, Y.; Li, Z.; Hu, J.; Wang, D.; Li, H.; Xi, K. Regulating relative nitrogen locations of diazine functionalized covalent organic frameworks for overall H<sub>2</sub>O<sub>2</sub> photosynthesis. *Angew. Chem., Int. Ed.* **2023**, *62* (41), No. e202310556.